



Effects of non-isothermal annealing on microstructure and mechanical properties of severely deformed 2024 aluminum alloy

Saeed KHANI MOGHANAKI, Mohsen KAZEMINEZHAD

Department of Materials Science and Engineering, Sharif University of Technology,
Azadi Avenue 11155-9466, Tehran, Iran

Received 25 January 2016; accepted 20 September 2016

Abstract: Microstructure and mechanical properties of AA2024 after severe plastic deformation (SPD) and non-isothermal annealing were investigated. The non-isothermal treatment was carried out on the severely deformed AA2024, and the interaction between restoration and precipitation phenomena was investigated. Differential scanning calorimetry, hardness and shear punch tests illustrate that static recovery and dissolution of GPB zones/Cu–Mg co-clusters occur concurrently through non-isothermal annealing. Scanning electron microscope and electron backscatter diffraction illustrate that non-isothermal annealing of deformed AA2024 up to 250 °C promotes the particle-free regions and also particle stimulated nucleation. Results show that through heating with the rate of 10 °C/min up to 250 °C, the ultimate shear strength and the hardness are maximum due to the presence of *S/S* phases which have been detected during non-isothermal differential scanning calorimetry experiment. Also, recrystallization phenomenon occurs in temperature range which includes the dissolution of *S/S* phases. The concurrent recrystallization and dissolution of *S/S* phase at 380 °C have been verified by differential scanning calorimetry, mechanical properties, and optical microscope.

Key words: AA2024 alloy; severe plastic deformation; non-isothermal annealing; microstructure; mechanical properties

1 Introduction

Interest in the production of ultra-fine grained bulk metals through severe plastic deformation processes has been grown in the last decades [1]. Multi-directional forging (MDF), as a severe plastic deformation method, can be used to produce ultra-fine grained bulk metals [1]. KIM et al [2] investigated the low temperature ageing effects on the mechanical properties of AA2024 alloy after equal channel angular pressing (ECAP). Their research illustrated that solution treatment prior to ECAP and post low temperature ageing improved the strength and the ductility of equal channel angular pressed AA2024 alloy. The dissolution of second phase during severe plastic deformation can occur and this can change the ageing behavior of aluminum alloy [3]. MURAYAMA et al [3] investigated the dissolution behavior of θ' phases during ECAP in Al–Cu binary alloy. Also, LIU et al [4] measured the dissolution content of θ' in Al–Cu during ECAP and MDF processes. Their results suggested that θ' phase in the multi-directional forged sample dissolved more rapidly than

that in the equal channel angular pressed sample and they attributed this difference to stress state between ECAP and MDF. KANG et al [5] studied the initial heat treatment effect on the mechanical properties of equal channel angular pressed AA2024. They demonstrated that the hardness of equal channel angular pressed samples in super saturated solid solution AA2024 alloy is higher than that of equal channel angular pressed samples in peak-aged and over-aged conditions and this is due to the dynamic precipitation occurrence during ECAP [5].

However, many works have been carried out on the isothermal annealing of severely deformed metals and alloys, and most of the heat treatments performed on the age hardenable aluminum alloys after severe plastic deformation are isothermal [6–11]. For example, LEE et al [12] illustrated that by severe plastic deformation and isothermal annealing at 373 K, AA7075 could achieve the ultimate tensile strength of ~600 MPa. Furthermore, in Al–4%Cu (mass fraction) alloy after high pressure torsion (HPT) and annealing at 353 K, the strength is further improved, but the thermal stability of HPT-processed sample is unsatisfactory because of fast

precipitation [13]. Through non-isothermal heat treatments, the samples experience a non-isothermal cycle before the temperature reaches the target temperature. Thus, the behavior of materials before reaching isothermal temperature is important and must be known, especially for severely deformed materials in which the precipitation and restoration phenomena may occur at higher kinetics. HUANG et al [14,15] studied the effect of microchemistry of Mn and the concurrent precipitation during non-isothermal annealing and two-stage annealing on the microstructure and the mechanical properties of cold-rolled Al–Mn–Fe–Si. They found that the nucleation and growth of grains strongly depend on the microchemistry and annealing temperature. The heating rate effect on the recrystallization and concurrent precipitation in Al–Mn alloy was investigated by HUANG and MARTHINSEN [16] and it was found that increasing the heating rate leads to finer grain size, and the dominant texture component depends on the concurrent precipitation which is defined by heating rate. During welding, the materials also experience the non-isothermal condition. GENEVOIS et al [17] investigated the precipitation and mechanical behavior of AA2024 alloy during friction stir welding (FSW) in which the temperature history and deformation rate in weld zone are varied. By quantification of the microstructure, they developed a model for yield strength evolution during welding. Non-isothermal ageing differs in a number of ways from the classically studied isothermal precipitation: 1) during non-isothermal ageing, all parameters such as nucleation barriers and driving force of diffusion are evolved simultaneously. Thus, precipitates which nucleate at a given time step may be unstable in the next time step; 2) the nature and composition of phases may change with temperature during non-isothermal ageing, and 3) depending on the temperature history, nucleation sites may have limited stability, this is important when precipitates form on the pre-existence precipitates or clusters which may dissolve during heating ramps [18,19]. In addition to precipitation phenomena, restoration phenomena, recovery and recrystallization can occur in severely deformed aluminum alloy during non-isothermal annealing. Thus, it is necessary to investigate the interaction between restoration and precipitation phenomena which occur

during non-isothermal annealing. In non-isothermal experiment, heating rate is one of the important parameters which influences the precipitation, recovery and recrystallization phenomena [20]. For instance, a research carried out on the AA6061-T4 illustrated that heating rate increasing shifts the peak ageing temperature to the higher temperatures and the maximum hardness is decreased due to the formation of coarse β'' at high temperatures [21]. The similar results were reported by DAOUDI et al [22] in Al–Mg–Si alloy.

Since there are limited studies on the non-isothermal annealing of severely deformed age hardenable aluminum alloys, in this research, the non-isothermal annealing of severely deformed super saturated aluminum alloy 2024 is investigated, and the interaction between recovery, recrystallization and precipitation phenomena is studied.

2 Experimental

The chemical composition of 2024 aluminum alloy used in this research is given in Table 1. The rectangular cubic samples with initial dimensions of 10 mm × 10 mm × 15 mm were cut from cold-rolled billet (Fig. 1). In order to reduce the dislocation density from manufacturing history of the alloy, isothermal annealing was carried out at 420 °C for 2.5 h in the electrical furnace and then cooled to room temperature in the furnace. The samples were solution-treated at 495 °C for 1.5 h following by room temperature water quenching. To inhibit natural ageing, just after the solution treatment, the two-dimensional multi-directional forging was carried out on the samples at room temperature. In plane or two dimensional multi-directional forging, the compression force was applied only on two specific planes. In the first stage or pass of MDF, the compression force was applied on the first plane and in the next pass

Table 1 Chemical composition of investigated AA2024 alloy (mass fraction, %)

Al	Si	Fe	Cu	Mn
Base	0.112	0.348	3.86	0.449
Mg	Cr	Ni	Zn	
1.23	0.0195	0.0172	0.297	

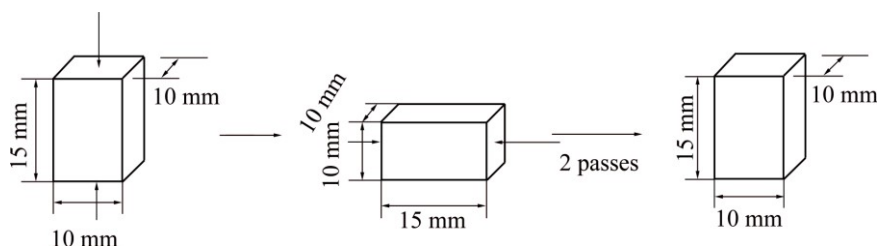


Fig. 1 Schematic of MDF process

the compression force was applied on the second plane and this sequence was repeated. The strain in the normal direction of third plane was zero. MoS₂ spray was used as a lubricant to reduce forging force. In this research, only two passes of MDF were performed on the samples and further straining led to failure. The strain after each pass was calculated by the following equation:

$$\varepsilon = \frac{2}{\sqrt{3}} \ln\left(\frac{H}{W}\right) \quad (1)$$

where H and W are the height and the width of the MDF samples, respectively. Just after multi-directional forging, the samples were heated with the heating rates of 10 and 200 °C/min up to 100, 180, 250, 320, and 380 °C and then quenched. To be sure that the temperature distribution of the samples is uniform during non-isothermal annealing, the samples were provided in small size (10 mm × 10 mm × 7.5 mm) and the thermocouple wires were located in the center of the samples. To evaluate the mechanical properties after non-isothermal

annealing, shear punch and hardness tests were carried out. The Vickers indenter was selected and the load was 20 kg. Differential scanning calorimetry (DSC), optical microscope, field emission scanning electron microscope (FE-SEM), and electron backscatter diffraction (EBSD) were used to study the microstructural evolution. For EBSD measurement, specimen surfaces were ground and polished according to standard metallographic technique, and then the samples were electro-polished in a solution of 30% nitric acid (volume fraction) and methanol at 30 V for 20 s. To reveal the microstructure under optical microscope, after grinding and polishing, the samples were electro-etched in solution of 3% HBF₄ (volume fraction) and distilled water at 20 V for 60 s.

3 Results and discussion

The optical microscopy images of non-isothermally annealed samples are shown in Fig. 2. In Fig. 2(a), the optical micrograph of multi-directional forged sample

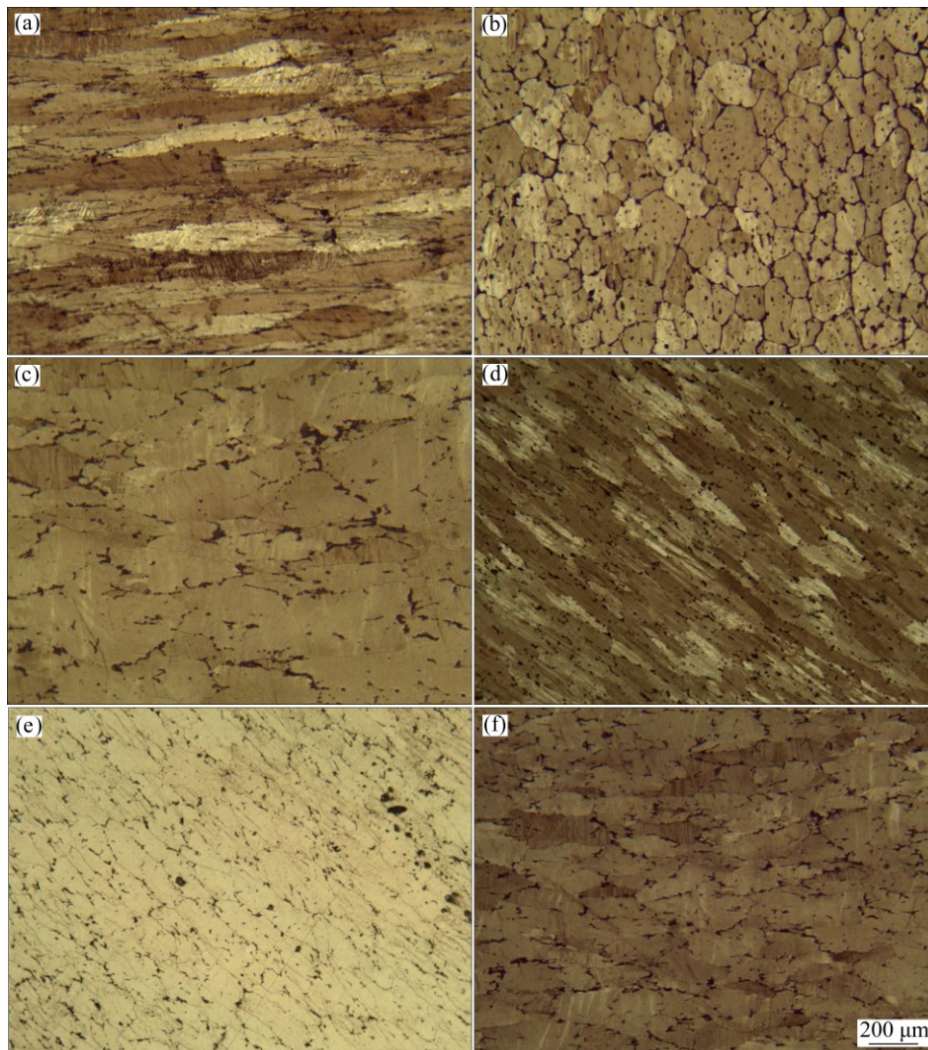


Fig. 2 Optical micrographs of two passes multi-directional forged samples: (a) Without annealing; (b) Annealed up to 250 °C with heating rate of 10 °C/min; (c) Annealed up to 380 °C with heating rate of 10 °C/min; (d) Annealed up to 100 °C with heating rate of 200 °C/min; (e) Annealed up to 250 °C with heating rate of 200 °C/min; (f) Annealed up to 380 °C with heating rate of 200 °C/min

after 2 passes is shown and an elongated pattern can be observed. Non-isothermal annealing of deformed sample up to 250 °C with the heating rate of 10 °C/min leads to an equiaxed pattern of formation in the microstructure after electro-etching (Fig. 2(b)). The exact investigation of this image (Fig. 2(b)) has been done by SEM. SEM images before and after electro-etching are shown in Fig. 3. Based on Figs. 3(a) and (b), before electro-etching during non-isothermal annealing up to 250 °C, some particle/precipitate-free regions appear in the microstructure and some intermetallics like $\text{Al}_7\text{Cu}_2\text{Fe}$ can be observed along these regions. The presence of $\text{Al}_7\text{Cu}_2\text{Fe}$ is confirmed by EDS and elemental map (Fig. 4). Thus, there are some particle-free regions with embedded intermetallics at 250 °C. The presence of particle-free zones in Al–Cu–Mg alloy at 260 °C was already confirmed by KHAFIZOVA et al [23], when they annealed the quenched sample at 260 °C. They observed formation of particle-free zones with 500 nm in width at grain boundaries, while in this study the width of these

regions is 3–6 μm . This larger width of particle-free can be attributed to presence of deformation in this case, because deformation can produce vacancy and these excess vacancies promote the formation of particle-free zones. After electro-etching due to more corrosion of particle-free regions, some boundaries appear in the

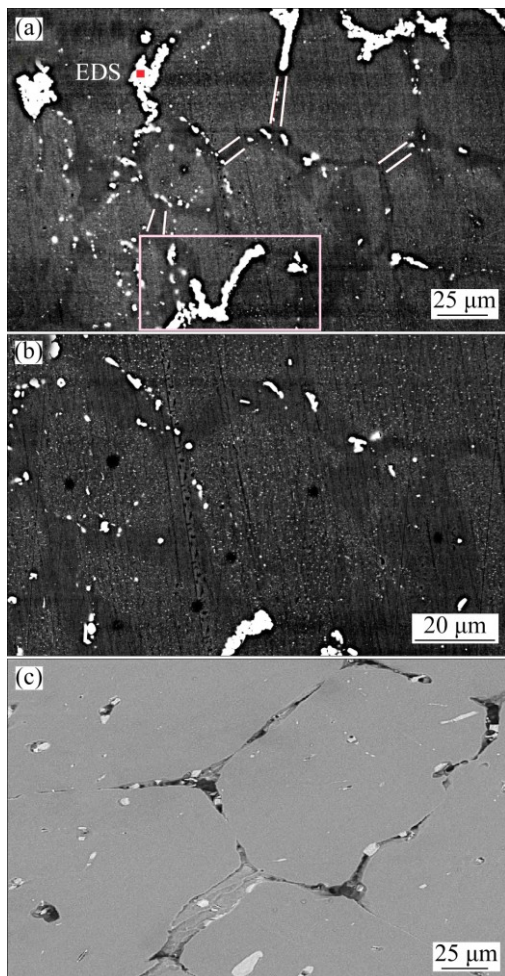


Fig. 3 SEM images of sample annealed up to 250 °C with heating rate of 10 °C/min: (a) Before electro-etching at lower magnification; (b) Before electro-etching at higher magnification; (c) After electro-etching (FE-SEM image)

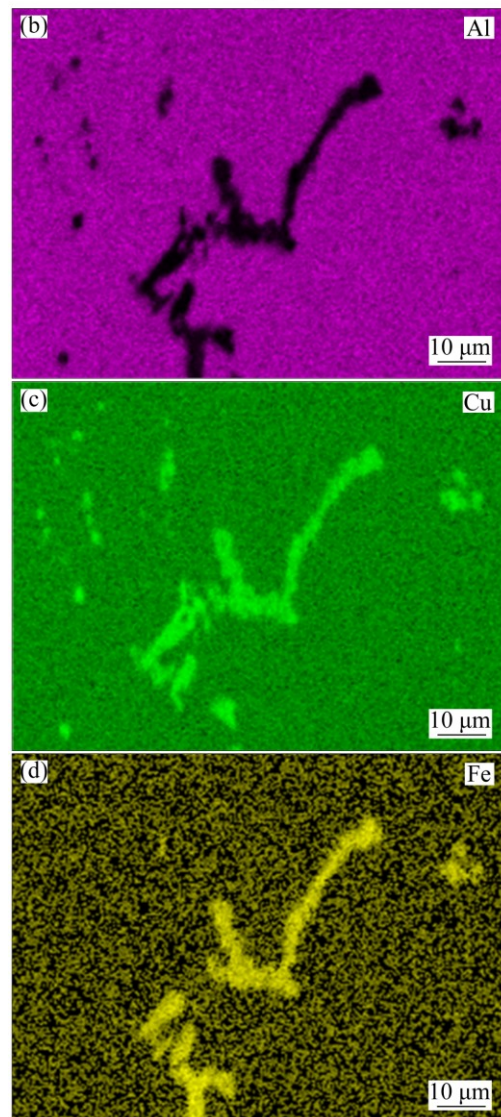
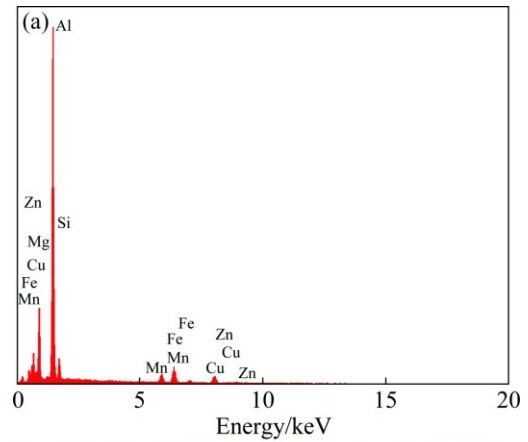


Fig. 4 Energy dispersive spectroscopy and elemental maps of marked point and area in Fig. 3(a)

microstructure (Fig. 2(b) and Fig. 3(c)). Further non-isothermal annealing up to higher temperature (380 °C) leads to no presence of particle-free zones and there are just some $\text{Al}_7\text{Cu}_2\text{Fe}$ (Fig. 2(c)).

Figure 2(d) shows the micrograph of a sample which is heated up to 100 °C with heating rate of 200 °C/min. The elongated pattern can be seen in this figure. Figure 2(e) shows the optical micrograph of a sample which is non-isothermally annealed up to 250 °C with heating rate of 200 °C/min. Comparison between Figs. 2(b) and (e) shows that at higher heating rate, there are yet elongated grains. Also, both particle-free region formation and precipitation of stable phases (based on Ref. [24]) are postponed with increasing the heating rate. In Fig. 2(f), after non-isothermal annealing up to 380 °C with the heating rate of 200 °C/min, equiaxed grains can be observed.

In Fig. 5, the differential scanning calorimetry curves of undeformed solution treated and multi-directional forged sample are shown (the scanning rate of DSC was 10 °C/min). Generally, there are four peaks in the DSC curve of undeformed sample, among which two peaks are exothermic and two peaks are endothermic. The first exothermic peak (40–120 °C) is related to GPB zones/Cu–Mg co-clusters formation and the following endothermic peak (120–250 °C) is related to the dissolution of these clusters [25]. The peak which appears in the temperature range of 250–300 °C belongs to S'/S phase formation and following endothermic peak is attributed to this phase dissolution [25]. Due to the dynamical formation of GPB zones/Cu–Mg co-clusters during severe plastic deformation, in Fig. 5, the first exothermic peak of deformed sample is eliminated and no further zones or clusters precipitate during DSC test. The dynamic formation of GPB zones during cycling plastic deformation of age-hardenable aluminum alloys was reported previously [26].

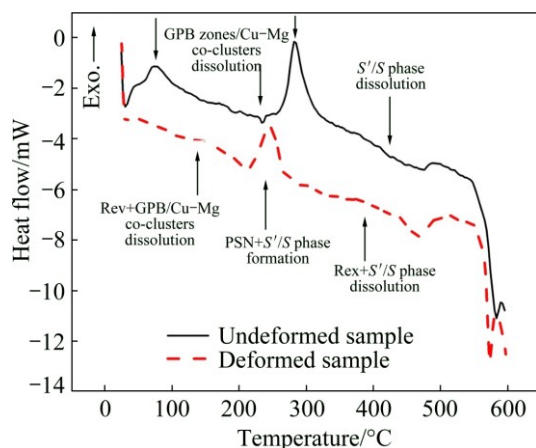


Fig. 5 DSC curves of solution-treated undeformed and two passes multi-directional forged samples (heating rate is 10 °C/min)

In Fig. 5, the comparison between the DSC curves of deformed and undeformed samples shows that however the dissolution peak of GPB zones/Cu–Mg co-clusters in deformed sample has a limited temperature range (160–230 °C), in undeformed sample, it has a sluggish peak with wide temperature range (110–250 °C). This limited temperature range of dissolution peak of deformed sample means that the static recovery as an exothermic phenomenon occurs, too. Since static recovery shifts the heat flow values to more exothermic values, the dissolution peak of zones/co-clusters in DSC curve of deformed sample appears in a limited temperature range. Thus, there is an interaction between the dissolution of GPB zones/Cu–Mg co-clusters and the static recovery during non-isothermal annealing. This interaction will be verified by change in ultimate shear strength and hardness in this temperature range. Since the dissolution of meta-stable phases occurs during non-isothermal annealing in the temperature range of 120–250 °C, the Cu and Mg concentrations are increased in the matrix. Due to the solute drag force on the dislocations, this solute content increasing in the matrix can inhibit the static recovery progressing with increasing the temperature. This is a strong effect of solute atoms on the static recovery and due to this effect, static recovery is not significantly observed at temperatures higher than 200 °C.

As seen in Fig. 5, the peak temperature of S'/S phase formation is at 290 °C in the undeformed sample. In the deformed sample, since the dislocation density and the vacancy content of deformed structure are high, the peak temperature of S'/S phase formation shifts to lower temperature of about 250 °C. Moreover, there is an exothermic peak at 380 °C in DSC curve of deformed sample which corresponds to recrystallization phenomenon. In Fig. 5, since the recrystallization peak appears in the temperature range of S'/S phase dissolution [27], the sluggish dissolution peak of the undeformed sample is observed as a sharp dissolution peak in the deformed sample. This exothermic peak of recrystallization has been reported in AA2024 alloy previously in the temperature range of 350–450 °C [27]. Since in the recrystallization phenomenon, the crystalline defects density is reduced, the recrystallization acts as an exothermic effect. Thus, there is an interaction between recrystallization and dissolution of S'/S phase.

An exact examination of the sample which was heated up to 250 °C with heating rate of 10 °C/min is carried out by EBSD. Figure 6 shows the EBSD maps of the deformed and annealed samples up to 250 °C. In Figs. 6(a) and (b), the orientation map and high-angle grain boundaries (HAGBs) for deformed sample are illustrated, respectively. Elongated patterns can be observed in these images. After non-isothermal

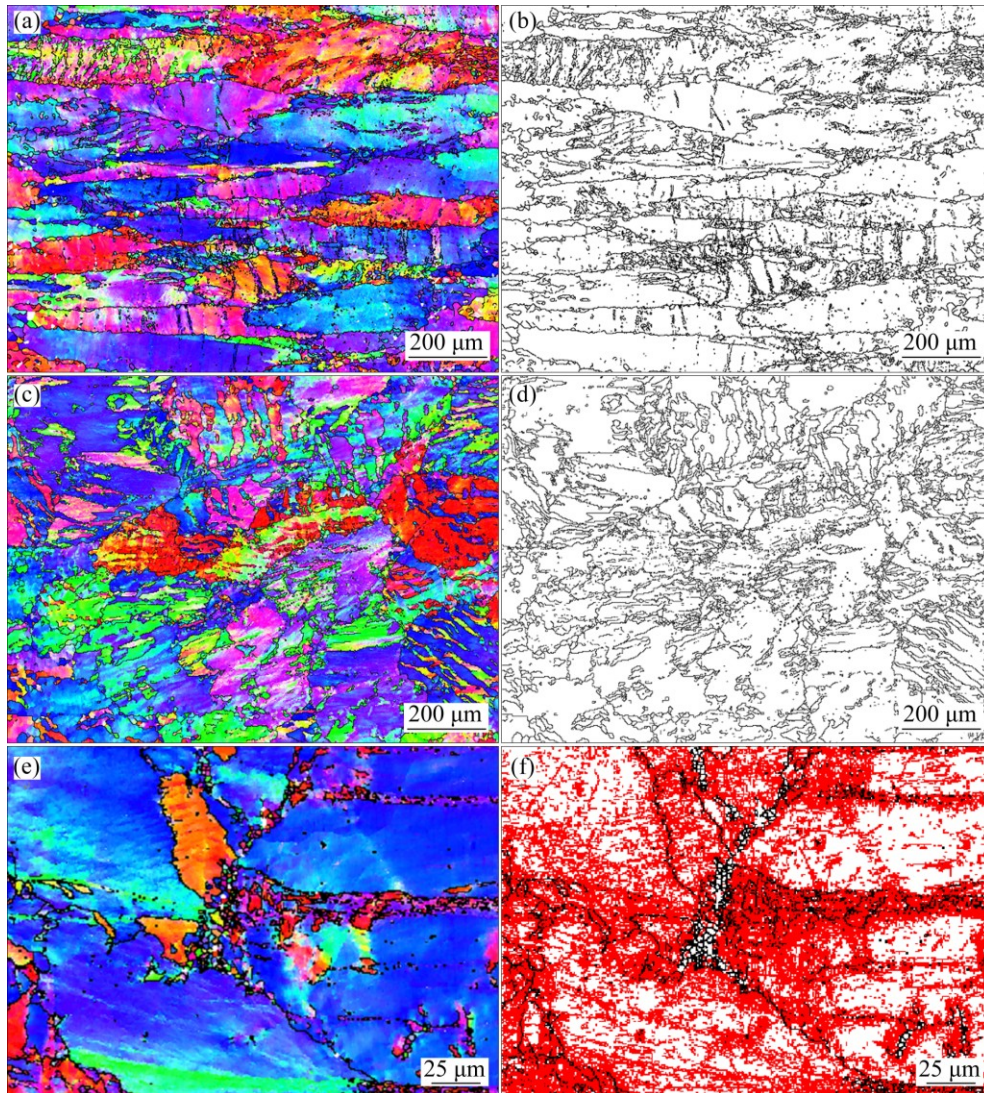


Fig. 6 EBSD analysis results: (a, b) EBSD map and grain boundary image of alloy after deformation (two MDF passes); (c, d) EBSD map and grain boundary image of alloy after non-isothermal annealing up to 250 °C with heating rate of 10 °C/min at low magnification; (e, f) EBSD map and grain boundary image of alloy after non-isothermal annealing up to 250 °C with heating rate of 10 °C/min at higher magnification (misorientation angles are presented as: red, 2°–15°; black >15°)

annealing up to 250 °C with heating rate of 10 °C/min, the EBSD map was obtained at both low and high magnifications. Figures 6(c) and (d) illustrate the orientation map and HAGBs at lower magnification for annealed sample, respectively, and Figs. 6(e) and (f) illustrate these maps at higher magnification. It is worth mentioning that in Fig. 6(f), the low-angle grain boundaries (LAGBs) is shown by red lines. Based on Figs. 6(e) and (f), there are some regions where small grains exist. These regions are the deformation zones adjacent to the particles like $\text{Al}_7\text{Cu}_2\text{Fe}$ that the sizes of these particles are more than 1 μm . During deformation, large particles induce the strain path changes in their vicinity and they can stimulate the nucleation of recrystallized grains, because of more stored energy in the deformation zones adjacent to the particles. This

phenomenon is called particle stimulated nucleation (PSN), and it is activated when there are particles with diameter larger than 1 μm in the microstructure [28]. The boundary misorientation distributions for the deformed sample and the annealed sample up to 250 °C are shown in Fig. 7. An obvious feature of these results is the much larger fraction of LAGBs present in the both conditions. In Fig. 7(a), there are only a few boundaries exceeding 40° in misorientation. This suggests that even at very low temperatures of annealing (250 °C), new very high misorientation boundaries are rapidly produced and this may be related to the strong effect of PSN.

Figure 8 shows the ultimate shear strength (USS) evolution during non-isothermal annealing of deformed alloy at different heating rates (HR) and temperatures. Three regions are shown in Fig. 8 that each region shows

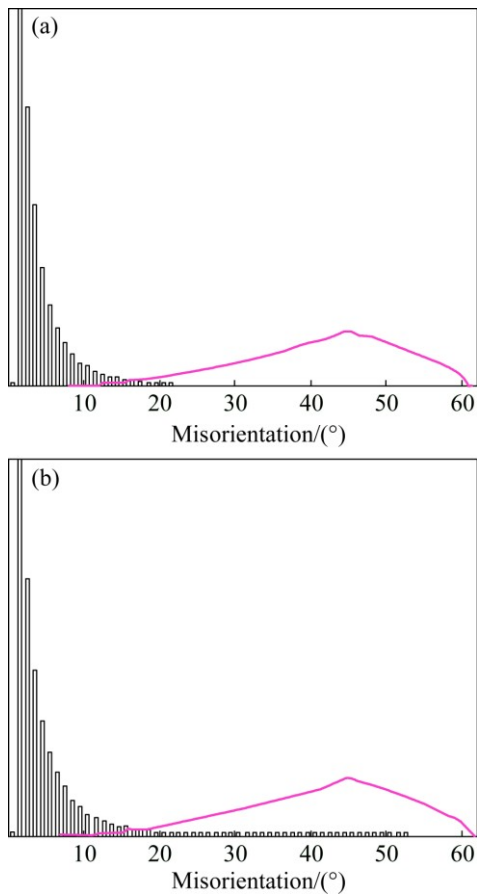


Fig. 7 Boundary misorientation distributions for alloy after deformation (two MDF passes) (a), and after non-isothermal annealing up to 250 °C (heating rate is 10 °C/min) (b)

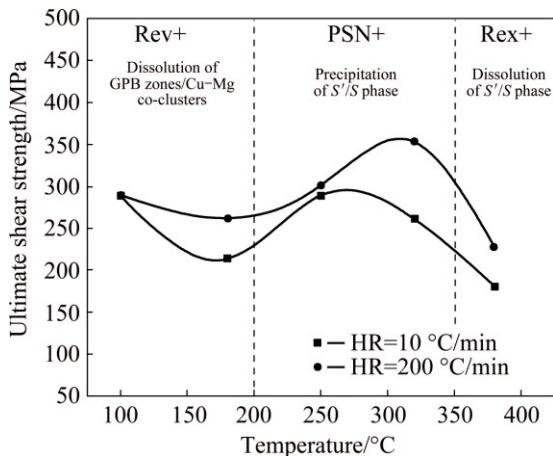


Fig. 8 Change in ultimate shear strength as function of non-isothermal annealing temperature and heating rate

the interaction between two phenomena which are described based on DSC and microscopy results mentioned above. In the first region, the USS drop is due to static recovery and dissolution of GPB zones/Cu–Mg co-clusters that occur simultaneously. In the second region, PSN and precipitation of S'/S phase occur and due to precipitation of S'/S phase the USS is increased.

With further annealing, in the third region, since dissolution of S'/S phase occurs, the USS is decreased. Also, in the third region, occurrence of both the recrystallization and the grain growth can lead to USS drop. It should be noted that the maximum strength in second region for heating rate of 200 °C/min occurs at higher temperature with respect to that for 10 °C/min. Also, in Fig. 8, the heating rate effect is obvious on the value of USS and this figure shows that the USS value is higher at higher heating rate. This is attributed to the retardation of recrystallization phenomenon, formation and dissolution of S'/S phase at higher heating rate.

In Fig. 9, the hardness evolution during non-isothermal annealing after two passes of MDF is shown. The similar trend to shear punch test results (Fig. 8) can be seen in this figure which confirms the descriptions mentioned above.

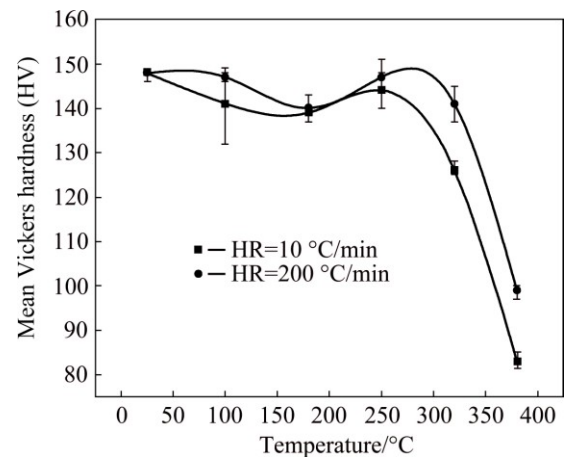


Fig. 9 Change in Vickers hardness as function of non-isothermal annealing temperature and heating rate

4 Conclusions

1) During non-isothermal annealing, the interaction between static recovery and dissolution of meta-stable phases such as GPB zones/Cu–Mg co-clusters occurs. The hardness test, shear punch test, and differential scanning calorimetry results verify this interaction in temperature range of 100–200 °C.

2) Based on the differential scanning calorimetry results, since the precipitation of S'/S phase occurred in temperature range of 200–325 °C, the hardness and ultimate shear strength were increased with increasing the temperature. During non-isothermal annealing up to 250 °C with 10 °C/min, some particle-free regions of 3–6 μm in width were revealed in the microstructure. Also, EBSD results showed that there are a few new formed high angle grain boundaries adjacent to intermetallic particles like Al_7Cu_2Fe (particle stimulated nucleation).

3) By further annealing up to higher temperatures

like 380 °C, both dissolution of S/S phase and recrystallization occurred and these led to the decrease of mechanical properties. The dissolution of S/S phase and the recrystallization at this temperature were recognized by DSC peaks.

4) During non-isothermal annealing, with increasing the heating rate, the recrystallization phenomenon, formation and dissolution of S/S phase are postponed.

Acknowledgments

The authors wish to thank the research board of Sharif University of Technology for the financial support and the provision of the research facilities used in this work. Also, they would like to thank Prof. Dr. Roland LOGÉ from EPFL for the use of his electron back scatter diffraction facility.

References

- [1] VALIEV R Z, ESTRIN Y, HORITA Z, LANGDON T G, ZEHETBAUER M J, ZHU Y T. Producing bulk ultrafine grained materials by severe plastic deformation [J]. *Journal of Minerals, Metals, and Materials Society*, 2006, 58: 33–39.
- [2] KIM W J, CHUNG C S, MA D S, HONG S I, KIM H K. Optimization of strength and ductility of 2024 Al by equal channel angular pressing (ECAP) and post-ECAP aging [J]. *Scripta Materialia*, 2003, 49(4): 333–338.
- [3] MURAYAMA M, HORITA Z, HONO K. Microstructure of two-phase Al–1.7 at% Cu alloy deformed by equal-channel angular pressing [J]. *Acta Materialia*, 2001, 49: 21–29.
- [4] LIU Z, CHEN X, HAN X, GU Y. The dissolution behavior of θ' phase in Al–Cu binary alloy during equal channel angular pressing and multi-axial compression [J]. *Materials Science and Engineering A*, 2010, 527: 4300–4305.
- [5] KANG S B, LIM C Y, KIM H W, MAO J. Microstructure evolution and hardening behavior of 2024 aluminum alloy processed by severe plastic deformation [J]. *Materials Science Forum*, 2002, 396–402: 1163–1168.
- [6] VASEGHI M, KIM H S. A combination of severe plastic deformation and ageing phenomena in Al–Mg–Si alloys [J]. *Materials and Design*, 2012, 30: 1894–1901.
- [7] MURASHKIN M Y, SABIROV I, MEDVEDEV A E, ENIKEEV N A, LEFEBVRE W, VALIEV R Z, SAUVAGE X. Mechanical and electrical properties of an ultrafine grained Al–8.5wt.% RE (RE=5.4wt.% Ce, 3.1wt.% La) alloy processed by severe plastic deformation [J]. *Materials and Design*, 2016, 90: 433–442.
- [8] SARKARI KHORRAMI M, KAZEMINEZHAD M, KOKABI A H. Thermal stability during annealing of friction stir welded aluminum sheet produced by constrained groove pressing [J]. *Materials and Design*, 2013, 45: 222–227.
- [9] SARKARI KHORRAMI M, KAZEMINEZHAD M, KOKABI A H. Thermal stability of aluminum after friction stir processing with SiC nanoparticles [J]. *Materials and Design*, 2015, 80: 41–50.
- [10] MOHAMED I F, YONENAGA Y, LEE S, EDALATI K, HORITA Z. Age hardening and thermal stability of Al–Cu alloy processed by high-pressure torsion [J]. *Materials Science and Engineering A*, 2015, 627: 111–118.
- [11] FARSHIDI M H, KAZEMINEZHAD M, MIYAMOTO H. Severe plastic deformation of 6061 aluminum alloy tube with pre and post heat treatments [J]. *Materials Science and Engineering A*, 2013, 563: 60–67.
- [12] LEE S, TAZOE K, MOHAMED I F, HORITA Z. Strengthening of AA7075 alloy by processing with high-pressure sliding (HPS) and subsequent aging [J]. *Materials Science and Engineering A*, 2015, 628: 56–61.
- [13] MOHAMED I F, YONENAGA Y, LEE S, EDALATI K, ZENJI J. Age hardening and thermal stability of Al–Cu alloy processed by high-pressure torsion [J]. *Materials Science and Engineering A*, 2015, 627: 111–118.
- [14] HUANG K, ENGLER O, LI Y J, MARTHINSEN K. Evolution in microstructure and properties during non-isothermal annealing of a cold-rolled Al–Mn–Fe–Si alloy with different microchemistry states [J]. *Materials Science and Engineering A*, 2015, 628: 216–229.
- [15] HUANG K, ZHAO Q, LI Y, MARTHINSEN K. Two-stage annealing of cold-rolled Al–Mn–Fe–Si alloy with different microchemistry states [J]. *Journal of Materials processing Technology*, 2015, 221: 87–99.
- [16] HUANG K, MARTHINSEN K. The effect of heating rate on the softening behavior of a deformed Al–Mn alloy with strong and weak concurrent precipitation [J]. *Materials Characterization*, 2015, 110: 215–221.
- [17] GENEVOIS C, DESCHAMPS A, DENQUIN A, DOISNEAU-COTTIGNIES B. Quantitative investigation of precipitation and mechanical behavior for AA2024 friction stir welds [J]. *Acta Materialia*, 2005, 53: 2447–2458.
- [18] DESCHAMPS A, BLEY F, LAE L, DUMONT M, PERRARD F. Characterization and modeling of non-isothermal precipitation in metallic systems [J]. *Advance Engineering Materials*, 2006, 8: 1236–1239.
- [19] NICOLAS M, DESCHAMPS A. Characterization and modeling of precipitate evolution in an Al–Zn–Mg alloy during non-isothermal heat treatments [J]. *Acta Materialia*, 2003, 51: 6077–6094.
- [20] SCHAFER C, MOHLES V, GOTTSTEIN G. Modeling of non-isothermal annealing: Interaction of recrystallization, recovery, and precipitation [J]. *Acta Materialia*, 2011, 59: 6574–6587.
- [21] YAZDANMEHR M, BAHRAMI A, MOUSAVI ANIJAN S H. A precipitation-hardening model for non-isothermal ageing of Al–Mg–Si alloys [J]. *Computational Materials Science*, 2009, 45: 385–387.
- [22] DAOUDI M I, TRIKI A, REDJAIMIA A, YAMINA C. The determination of the activation energy varying with the precipitated fraction of β'' metastable phase in an Al–Si–Mg alloy using non-isothermal dilatometry [J]. *Thermochimica Acta*, 2014, 577: 5–10.
- [23] KHAFIZOVA E, ISLAMGALIEV R, KLEVTSOV G, MERSON E. Microstructure, strength and fatigue of an ultrafine-grained Al–Cu–Mg alloy [J]. *Materials Physics and Mechanics*, 2015, 24: 232–241.
- [24] KHAN I N, STARINK M J, YAN J L. A model for precipitation kinetics and strengthening in Al–Cu–Mg alloys [J]. *Materials Science and Engineering A*, 2008, 472: 66–74.
- [25] STARINK M J, GAO N, YAN J L. The origins of room temperature hardening of Al–Cu–Mg alloys [J]. *Materials Science and Engineering A*, 2004, 387–389: 222–226.
- [26] HUTCHINSON C R, de GEUSER F, CHEN Y, DESCHAMPS A. Quantitative measurements of dynamic precipitation during fatigue of an Al–Zn–Mg–(Cu) alloy using small-angle X-ray scattering [J]. *Acta Materialia*, 2014, 74: 96–109.
- [27] GAO N, STARINK M J, FURUKAWA M, HORITA Z, XU C, LANGDON T G. Evolution of microstructure and precipitation in heat-treatable aluminum alloys during ECA pressing and subsequent heat treatment [J]. *Materials Science Forum*, 2006, 503–504: 275–280.
- [28] HUMPHREYS F J, HATHERLY M. *Recrystallization and related annealing phenomena* [M]. 2nd ed. Amsterdam: Elsevier, 2004.

非等温退火对剧烈变形 2024 铝合金 显微组织和力学性能的影响

Saeed KHANI MOGHANAKI, Mohsen KAZEMINEZHAD

Department of Materials Science and Engineering, Sharif University of Technology,
Azadi Avenue 11155-9466, Tehran, Iran

摘要: 研究剧烈塑性变形和非等温退火 AA2024 合金的显微组织和力学性能。对剧烈塑性变形的 AA2024 合金进行非等温退火, 研究回复和析出之间的关系。差示扫描量热法、硬度和冲剪试验结果表明, 经过非等温退火处理, 静态回复和 GBP 区/Cu-Mg 团簇的溶解同时存在。扫描电子显微镜和背散射电子衍射结果表明, AA2024 合金非等温退火至 250 °C 促进了无沉淀区和粒子激发形核。通过 10 °C/min 加热至 250 °C, 由于 S/S' 相的存在, 合金的抗剪强度和硬度达到最大。差示扫描量热法、力学性能和光学显微镜结果表明, 加热至 380 °C 时, 再结晶和 S/S' 相的溶解共同存在。

关键词: AA2024 合金; 剧烈塑性变形; 非等温退火; 显微组织; 力学性能

(Edited by Yun-bin HE)